

Evaluation of a Land–Atmosphere Coupling Metric Computed from a Ground-Based Infrared Interferometer

RYANN A. WAKEFIELD,^a DAVID D. TURNER,^b AND JEFFREY B. BASARA^{a,c}

^a *School of Meteorology, University of Oklahoma, Norman, Oklahoma*

^b *NOAA/Global Systems Laboratory, Boulder, Colorado*

^c *School of Civil Engineering and Environmental Science, University of Oklahoma, Norman, Oklahoma*

(Manuscript received 16 December 2020, in final form 24 March 2021)

ABSTRACT: Land–atmosphere feedbacks are a critical component of the hydrologic cycle. Vertical profiles of boundary layer temperature and moisture, together with information about the land surface, are used to compute land–atmosphere coupling metrics. Ground-based remote sensing platforms, such as the Atmospheric Emitted Radiance Interferometer (AERI), can provide high-temporal-resolution vertical profiles of temperature and moisture. When collocated with soil moisture, surface flux, and surface meteorological observations such as at the Atmospheric Radiation Measurement (ARM) Southern Great Plains site, it is possible to observe both the terrestrial and atmospheric legs of land–atmosphere feedbacks. In this study, we compare a commonly used coupling metric computed from radiosonde-based data with that obtained from the AERI to characterize the accuracy and uncertainty in the metric derived from the two distinct platforms. This approach demonstrates the AERI's utility where radiosonde observations are absent in time and/or space. Radiosonde- and AERI-based observations of the convective triggering potential and low-level humidity index (collectively referred to as CTP-HI_{low}) were computed during the 1200 UTC observation time and displayed good agreement during both the 2017 and 2019 warm seasons. Radiosonde- and AERI-derived metrics diagnosed the same atmospheric preconditioning based upon the CTP-HI_{low} framework a majority of the time. When retrieval uncertainty was considered, even greater agreement was found between radiosonde- and AERI-derived classification. The AERI's ability to represent this coupling metric well enabled novel exploration of temporal variability within the overnight period in CTP and HI_{low}. Observations of CTP-HI_{low} computed within a few hours of 1200 UTC were essentially equivalent; however, with greater differences in time there arose greater differences in CTP and HI_{low}.

KEYWORDS: Boundary layer; Atmosphere-land interaction; In situ atmospheric observations; Remote sensing

1. Introduction

Land–atmosphere interactions play a critical role in both the atmospheric water and energy cycle. The sensitivity of the atmosphere to changes in land surface conditions is particularly pronounced in semiarid regions throughout the world (Guo et al. 2006; Koster et al. 2006; Dirmeyer 2006). Changes in soil moisture and vegetation health alter the partitioning of surface water and energy fluxes, influencing diurnal evolution of the planetary boundary layer (PBL), and even subsequent cloud and precipitation development. Along the same lines, persistence in soil moisture states may drive longer-term precipitation anomalies and geopotential height anomalies (Koster et al. 2016). As such, extreme events such as drought, heatwaves (Miralles et al. 2014; Schumacher et al. 2019), heavy rainfall (Wei et al. 2015; Song et al. 2016), or even the overland reintensification of tropical cyclones (Emanuel et al. 2008; Arndt et al. 2009; Andersen and Shepherd 2013; Andersen et al. 2013; Wakefield et al. 2021) can be impacted by land–atmosphere feedbacks. Greater understanding

of how the atmosphere and land surface covary, also referred to as land–atmosphere coupling (LA coupling), is essential to improving predictability of such extremes (Seneviratne et al. 2006; Koster et al. 2011; Dirmeyer and Halder 2016).

Numerical modeling approaches to study LA coupling range in scale from single column models (Ek and Mahrt 1994; Ek and Holtslag 2004) to atmospheric general circulation models (Dirmeyer 2001; Koster et al. 2004; Guo et al. 2006; Koster et al. 2006, 2014) to conceptualize the link between surface and atmospheric processes across scales. Observation-based studies (e.g., Basara and Crawford 2002; McPherson et al. 2004; Phillips and Klein 2014; Tang et al. 2018) supplement these approaches by quantifying the true behavior of these processes in nature and can inform more realistic representation of coupling in models. Coupling metrics arose from the need to succinctly quantify land–atmosphere feedbacks in both modeling and observational studies (Santanello et al. 2018). Numerous metrics have been developed by the LA-coupling community and exist on a spectrum of complexity. Process-level metrics describe multiple components of the local land–atmosphere coupling process chain (Santanello et al. 2011a,b), to better capture the multiple steps through which the land surface influences the evolution of the PBL and free atmosphere.

One frequently used process-level coupling metric is the convective triggering potential–low-level humidity index (CTP-HI_{low}) framework (Findell and Eltahir 2003a,b). This metric has been applied using its original formulation across multiple regions of the world (Jach et al. 2020). It has also been

Current affiliations for Wakefield: Cooperative Institute for Research in Environmental Sciences, University of Colorado, and NOAA/Global Systems Laboratory, Boulder, Colorado.

Corresponding author: Ryann A. Wakefield, ryann.wakefield@noaa.gov

DOI: 10.1175/JHM-D-20-0303.1

© 2021 American Meteorological Society. For information regarding reuse of this content and general copyright information, consult the AMS Copyright Policy (www.ametsoc.org/PUBSReuseLicenses).

modified based on climatology of the metric over various regions (Ferguson and Wood 2011; Wakefield et al. 2019) or to create a new diagnostic for land–atmosphere coupling contributions to hydroclimate extremes such as drought (Roundy et al. 2013; Roundy and Santanello 2017). The CTP-HI_{low} framework uses early morning vertical profiles to diagnose whether the atmosphere is preconditioned toward clouds and/or convective precipitation triggered over wet or dry soils (Findell and Eltahir 2003a,b). The use of the early morning radiosonde profiles was intended to represent the lower troposphere before substantial mixing of the PBL occurs. In the contiguous United States (CONUS), 1200 UTC typically corresponds to a preconvective boundary layer, between 0400 and 0800 local time (LT). However, in different regions of the world, neither of the synoptic radiosonde launches at 0000 UTC and 1200 UTC may coincide with the early morning PBL (i.e., perhaps they are in the middle of the night or they represent a well-mixed PBL in the day). One solution is to use vertical profiles corresponding to the same local time at every location. However, this approach is limited by the availability of vertical profiles during periods beyond the typical 1200 and 0000 UTC radiosonde observations.

To address this limitation, vertical profiles obtained from remote sensing platforms such as the Atmospheric Infrared Sounder (AIRS) on board NASA's *Aqua* satellite have been used to compute CTP and HI at the same local time (0130 LT) for locations around the world (Ferguson and Wood 2011; Roundy et al. 2013; Roundy and Santanello 2017). Because 0130 LT is consistent with a preconvective boundary layer, it was suggested that little difference should exist between vertical profiles obtained at 0130 LT and those obtained at 1200 UTC [which corresponds to a local time of 0700 central daylight time (CDT)] across the CONUS. Indeed, there was good agreement between computations of CTP and HI obtained from AIRS when compared with reanalysis datasets. Even so, a lack of ground-based observations with sufficient temporal resolution made it difficult to directly observe whether temporal variability does truly exist in CTP and HI during the period between the AIRS overpass time and the radiosonde observation time. Furthermore, thermodynamic profiles retrieved from infrared sounders like AIRS have relatively little information content in the PBL, resulting in coarse (e.g., order 1–2 km) vertical resolution (Irion et al. 2018). As such, we will explore the question of temporal variability of CTP and HI further in our study.

The lack of such studies until now is primarily driven by a lack of atmospheric profile observations at higher spatial and/or temporal frequencies than those offered by the traditional twice daily radiosonde observations. Ground-based thermodynamic profilers, such as the Atmospheric Emitted Radiance Interferometer (AERI), provide an alternative method for obtaining vertical profiles of temperature and moisture at higher temporal frequencies and where radiosonde observations are absent.

The AERI is a ground-based passive spectrometer that measures downwelling infrared radiation. Thermodynamic profiles are retrieved from the observed radiance data (the method is described in section 2b), but the vertical resolution is

lower than that of traditional radiosonde profiles. This decrease in vertical resolution introduces some uncertainty when using the AERI to compute convective indices, though these uncertainties are generally greatest for integrated indices such as convective available potential energy (CAPE) (Blumberg et al. 2017). Despite this limitation, the temporal resolution of the AERI makes it a useful tool for monitoring destabilization trends within the PBL (Feltz et al. 2003; Wagner et al. 2008; Blumberg et al. 2015, 2017) at temporal resolutions unmatched by radiosonde observations.

The temporal resolution of the AERI provides a unique opportunity to evaluate land–atmosphere coupling, in particular, and allows us to address several questions left unanswered by previous studies. The main questions we address in this study are

- 1) What are the uncertainties associated with computing CTP and HI from AERI profiles relative to collocated radiosonde profiles?
- 2) Do CTP and HI exhibit substantial temporal variability overnight, or are these values consistent as long as they are obtained for a preconvective PBL?

We focus our analyses at the Atmospheric Radiation Measurement (ARM) program's Southern Great Plains (SGP) site (Sisterson et al. 2016) in Lamont, Oklahoma, during the summers (June–August) of 2017 and 2019.

2. Data

a. Atmospheric Emitted Radiance Interferometer

The AERI measures downwelling radiance emitted from the atmosphere at wavelengths between 3.3 and 19.2 μm approximately twice per minute at 1 cm^{-1} spectral resolution (Knuteson et al. 2004a). The instrument maintains calibration by regularly observing two blackbodies, one at 60°C and one at ambient temperature, which results in the AERI maintaining its radiometric accuracy to better than 1% of the ambient radiance in both clear and cloudy conditions (Knuteson et al. 2004b). In the presence of precipitation, an automated hatch is closed to protect the foreoptics of the instrument.

b. AERIoe algorithm for thermodynamic profile retrieval

Retrieval algorithms are necessary to obtain thermodynamic profiles from the observed infrared radiance spectra. These algorithms make use of CO_2 and H_2O absorption bands that lie within the spectral range of the AERI to obtain temperature and water vapor profiles, respectively. The original retrieval algorithm AERIprof (Feltz et al. 1998; Smith et al. 1999) had several limitations including the inability to retrieve thermodynamic profiles under low- and midlevel clouds, which motivated the development of the AERIoe algorithm to address these shortcomings (Turner and Löhnert 2014; Turner and Blumberg 2019). The AERIoe algorithm retrieves thermodynamic profiles and cloud properties (e.g., liquid water path) from the AERI radiance observations using an optimal estimation (OE) framework (Rodgers 2000). This framework

allows for the uncertainties associated with each retrieved variable to be quantified, and these uncertainties can be propagated to provide uncertainties in the derived coupling metrics.

c. Site selection

While multiple AERI instruments are located in the ARM SGP domain, we use only the central facility (denoted sgpC1) AERI for this particular study as radiosondes are launched within 150 m of this AERI. This allows for coupling metrics to be derived from both AERI and radiosonde profiles and for the relative accuracy in the AERI-derived metrics to be quantified. This study used sgpC1 and 1200 UTC radiosonde data from three periods: 16 May to 12 June 2017, 1–31 August 2017, and 17 April to 31 August 2019. These three periods coincide with three different field campaigns at the ARM SGP site. The 16 May to 12 June 2017 period was in support of the Vaisala DIAL IOP (Newsom et al. 2020), the August 2017 period was in support of the Land–Atmosphere Feedback Experiment (LAFE; Wulfmeyer et al. 2018), and the 2019 period was in support of the Micropulse DIAL IOP.

3. CTP–HI analysis

a. Framework description

CTP–HI_{low} (hereinafter CTP–HI) was developed by Findell and Eltahir (2003a,b) to diagnose the preconditioning of the atmosphere toward locally triggered convection based upon whether soils are wet or dry. It was developed from the output of a one-dimensional model over Illinois and further tested using observational data from upper-air stations across the United States. The framework uses the 1200 UTC sounding data, which are within a few hours of sunrise in most locations within the continental United States, in order to determine the moisture content and instability within the portion of the atmosphere most likely to be incorporated into the growing mixed layer.

HI is computed from the sum of the dewpoint depressions at 50 and 150 hPa above ground level (AGL) to provide an estimate of the preexisting moisture in the atmosphere (°C):

$$HI = (T - Td)_{150\text{hPaAGL}} + (T - Td)_{50\text{hPaAGL}}, \quad (1)$$

where T is temperature and Td is dewpoint temperature. CTP is computed by locating the moist adiabat that intersects the temperature profile at 100 hPa above ground level and integrating the area between this moist adiabat and the temperature profile, upward within a 200-hPa layer from 100 hPa above ground level to 300 hPa above ground level. Units of CTP are joules per kilogram. This process assumes a saturated parcel at 100 hPa AGL. Pseudoadiabats (moist adiabats) were computed using the MetPy (May et al. 2020) software package that integrates the equation for moist adiabatic lapse rate obtained from Eq. (5) in Bakhshaii and Stull (2013). The computation of CTP is similar to that of CAPE. CTP estimates the instability within the layer of the atmosphere between 100 and 300 hPa AGL (approximately 1–3 km AGL). The combined

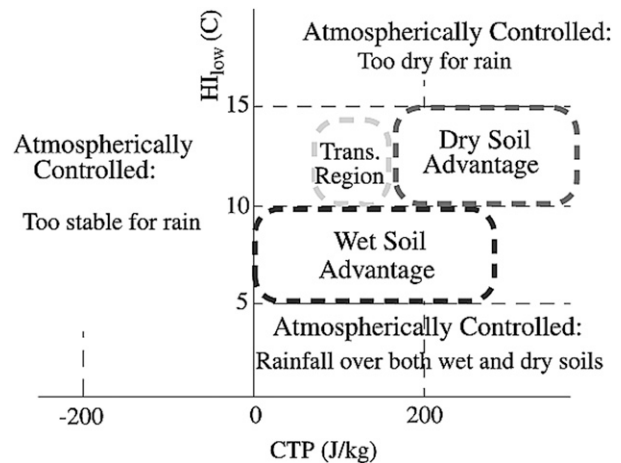


FIG. 1. Figure 15 from Findell and Eltahir (2003b) showing CTP–HI combinations for each category of atmospheric preconditioning.

CTP and HI pair can be used to diagnose whether convection is favored over wet or dry soils based upon thresholds set forth in Findell and Eltahir (2003a,b).

Based on this information, the atmosphere is classified into several different categories:

- 1) *atmospherically controlled*—This can either mean that if convection occurs, it is not locally triggered, or it can mean that the atmosphere is too stable or too dry for convective triggering. Therefore, this category has been divided into three subcategories based on Findell and Eltahir (2003a,b):
 - (i) *atmospherically controlled stable (ACst)*, where the atmosphere is too stable for precipitation (when $CTP < 0 \text{ J kg}^{-1}$),
 - (ii) *atmospherically controlled wet (ACw)*, where the atmosphere is already moist such that rainfall or shallow clouds can occur over any soil condition depending on CTP value ($HI < 5^\circ\text{C}$), and
 - (iii) *atmospherically controlled dry (ACd)*, where the atmosphere is too arid for convective precipitation to occur ($HI > 15^\circ\text{C}$).
- 2) *wet advantage (WA)*—Locally triggered convection is most likely over wet soils.
- 3) *dry advantage (DA)*—Locally triggered convection is most likely over dry soils.
- 4) *transition (T)*—Convection may occur over any soil type, but no convection is the most likely outcome. If convection is triggered, it is most likely over dry soils.

The numerical thresholds for each category are depicted in Fig. 15 of Findell and Eltahir (2003a) and are reproduced here in Fig. 1.

b. Uncertainties associated with AERI-derived CTP and HI

The framework uses morning vertical profiles from radiosondes, and in the western hemisphere, this corresponds to the 1200 UTC observation. While these are considered 1200 UTC observations, they are typically recorded in the hour between

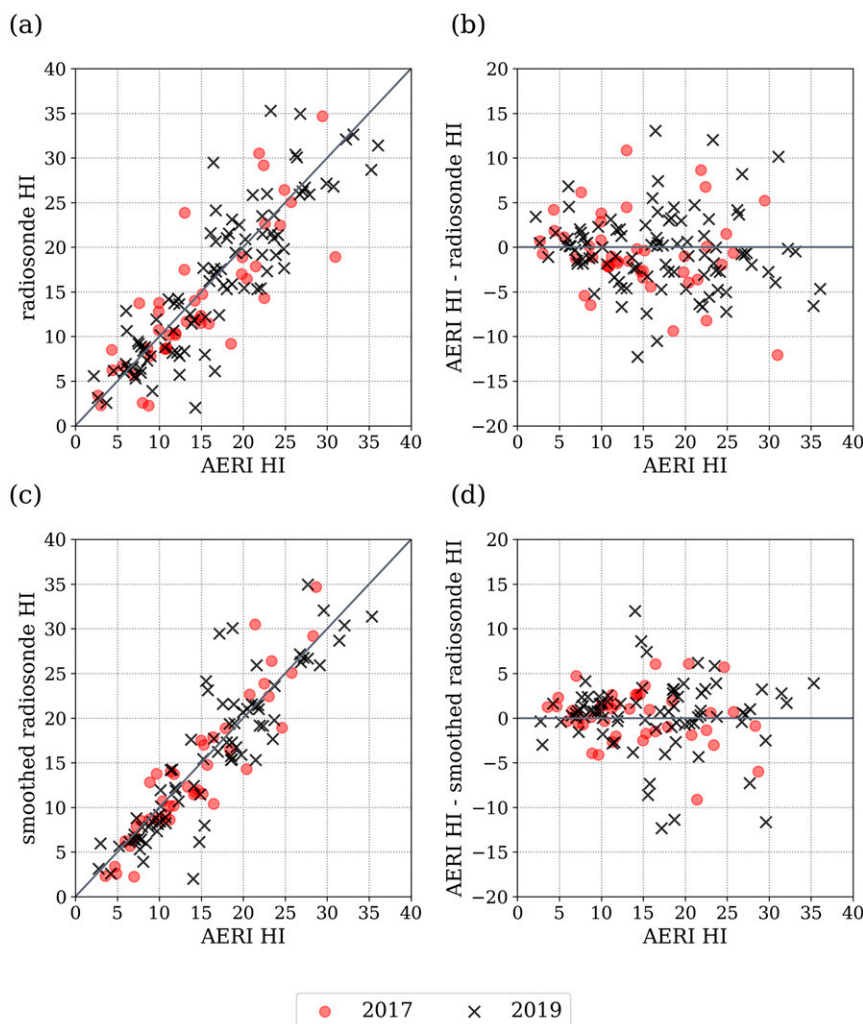


FIG. 2. (a) AERI HI vs radiosonde HI, (b) AERI HI vs AERI–radiosonde HI difference, (c) AERI HI vs smoothed radiosonde HI, and (d) AERI HI vs AERI–smoothed radiosonde HI difference. Black points represent 2017 data, and red points represent 2019 data.

1100 and 1200 UTC. Thus, the typical 1200 UTC radiosonde observation is often still within the boundary layer during the 1100 to 1200 UTC time window. As such, we selected AERI retrievals that occurred within the 1100–1200 UTC window that had both (i) small root-mean-square (RMS) error (i.e., the retrieved thermodynamic profile agrees well, in a radiance sense, with the radiance observations) and (ii) the retrieved liquid water path (LWP) was less than 6 g m^{-2} to ensure little to no overhead clouds. Of the retrievals that met the aforementioned criteria, the retrieval closest in time to radiosonde launch time was selected for comparison.

CTP and HI were computed from the selected AERI profile. Each AERI-retrieved profile has its associated uncertainties that can be used to approximate uncertainties in the CTP and HI values obtained from the profile. Using the posterior error covariance matrix produced by the AERLoe retrieval algorithm, uncertainties in the profile were then estimated by using Monte Carlo resampling of the posterior error covariance

matrix 500 times (similar to the approach used in [Blumberg et al. 2017](#)). This produced a distribution of 500 possible water vapor and temperature profiles. CTP and HI were then computed from each profile to obtain a distribution of possible CTP and HI observations at a given time.

We first compared CTP and HI observations obtained from the full vertical resolution of the radiosonde profiles with those obtained from the AERI thermodynamic profiles. [Figures 2a](#) and [3a](#) show that AERI-derived CTP and HI agreed well with HI and CTP values obtained from the radiosonde observations, respectively. The R^2 values computed using the Pearson correlation coefficient indicate that HI displayed slightly better agreement between the two platforms, with a slightly greater R^2 value than that of CTP ([Table 1](#)). When broken down by year, both years performed similarly.

One primary source of error in the AERI-retrieved versus radiosonde profiles arises due to differences in vertical resolution. Given the reduced vertical resolution in the AERI (see

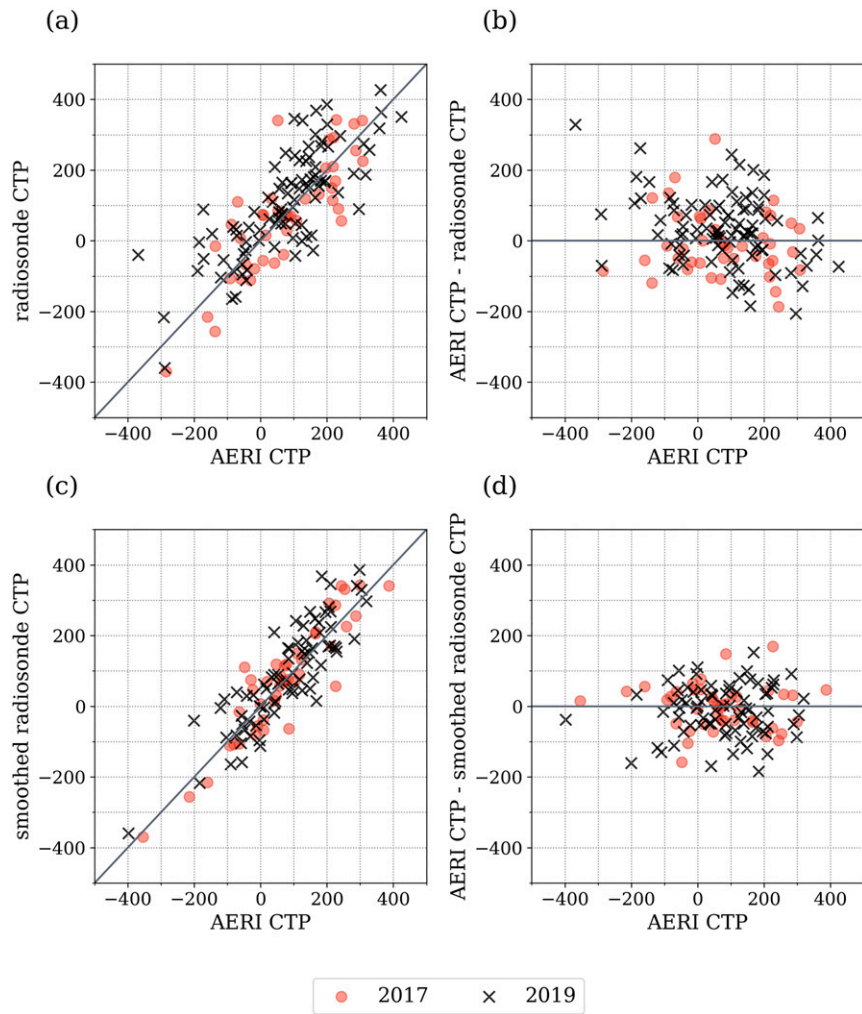


FIG. 3. As in Fig. 2, but for CTP.

Fig. 7 in Turner and Löhnert 2014) as compared with radiosonde profiles, differences in CTP and HI observed from each platform may be attributed to differences in vertical resolution. To test this theory, radiosonde profiles were smoothed to the same vertical resolution as the corresponding AERI profiles for the given time. This was completed using the averaging kernel produced by the AERIoe retrieval algorithm (Turner and Löhnert 2014). Reducing the vertical resolution of the radiosonde profiles produced CTP and HI values that were more similar to those obtained from the AERI (Figs. 2c and

3c). The improved agreement suggests that the unsmoothed radiosonde profiles and AERI profiles differ, in part, due to differences in vertical resolution. Overall, CTP showed a lower degree of covariability than HI in datasets for both years and for the smoothed and unsmoothed comparison.

c. Accuracy of preconditioning classifications

A primary objective of this study is to determine whether the AERI can serve as a useful tool for implementing the CTP-HI framework to diagnose atmospheric preconditioning

TABLE 1. The R^2 values computed from Pearson correlation for AERI vs radiosonde CTP and HI observations, bias, and standard deviation of the difference between AERI and radiosonde observations.

	R^2 2017 ($N = 43$)	R^2 2019 ($N = 95$)	R^2 both ($N = 138$)	Bias (both)	Std dev (both)
AERI vs radiosonde HI	0.64	0.66	0.65	-0.45°C	4.32°C
AERI vs smoothed radiosonde HI	0.75	0.86	0.83	-0.29°C	3.66°C
AERI vs radiosonde CTP	0.65	0.63	0.62	18.06 J kg^{-1}	98.73 J kg^{-1}
AERI vs smoothed radiosonde CTP	0.70	0.76	0.72	6.71 J kg^{-1}	71.67 J kg^{-1}

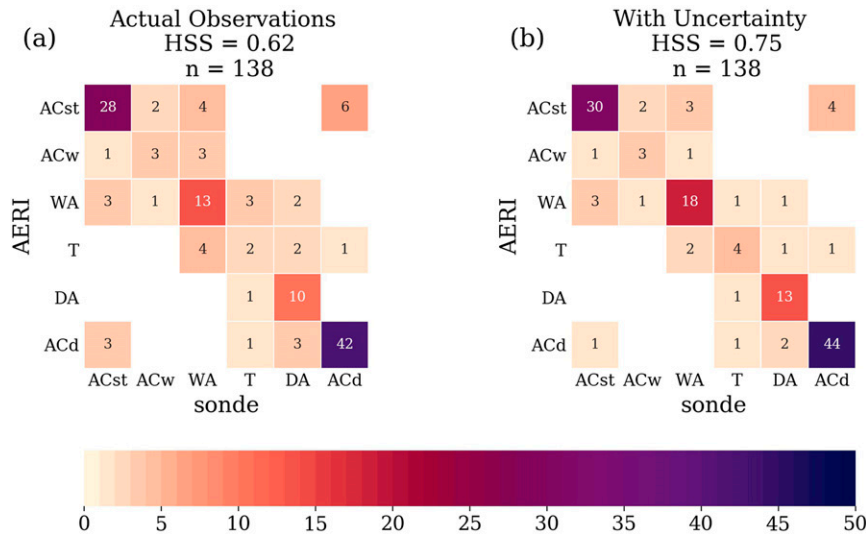


FIG. 4. Contingency matrix comparing CTP-HI classifications obtained based on radiosonde vs AERI CTP-HI observations and Heidke skill scores (a) without window of uncertainty and (b) including AERI window of uncertainty. The color bar corresponds to number of counts, and this number is also annotated directly within the matrix.

accurately. Therefore, we performed additional comparisons to values obtained from the unsmoothed radiosonde profiles. This allowed us to evaluate whether the AERI can provide the same diagnosis of atmospheric preconditioning via the CTP-HI framework as the radiosonde despite its lower vertical resolution. Hereinafter any reference to radiosonde profiles is referring to the unsmoothed radiosonde profiles.

The combination of CTP and HI observations for a given time were used to diagnose atmospheric preconditioning based upon discrete thresholds for each preconditioning category. Because of the discrete thresholds used in this coupling framework, small differences in CTP and HI between the AERI and radiosonde could result in a different classification of the atmospheric preconditioning. As such, we performed an additional comparison of the atmospheric preconditioning diagnosed by each instrument using the CTP-HI framework following the thresholds set forth in Findell and Eltahir (2003a,b). A 6×6 verification contingency table was created using the classification categories listed above, with Atmospherically Controlled (AC) conditions further separated into stable (ACst), wet (ACw), and dry (ACd) categories within the table (Fig. 4). AERI and radiosonde observations that produced the same classification reside along the diagonal, and off-diagonal elements represent differences in classification.

To diagnose the AERI's skill, we computed the Heidke skill score (HSS) using the approach in Wilks (2011):

$$\text{HSS} = \frac{\sum_{i=1}^I p(y_i, o_i) - \sum_{i=1}^I p(y_i)p(o_i)}{1 - \sum_{i=1}^I p(y_i)p(o_i)}, \quad (2)$$

where I represents the number of elements in the row or column and i is the i th element; $p(y_i, o_i)$ represents the joint distribution of AERI and radiosonde classifications, or diagonal elements of the table, and the individual AERI $p(y_i)$ and radiosonde $p(o_i)$ marginal distributions of observations represent the off-diagonal elements. In terms of forecast verification, an HSS of 1 represents a perfect forecast—that is, the AERI classifications perfectly matched the radiosonde classifications, and a score of 0 indicates that the same agreement between radiosonde and AERI classifications could be achieved by chance.

In addition, we considered all possible classifications within the retrieval's window of uncertainty. The window of uncertainty was defined as greater than or less than one-half standard deviation of the observed value based upon the distribution of potential profiles. CTP and HI were computed from each of the profiles within this window of uncertainty to diagnose atmospheric preconditioning. We also only considered the range of uncertainties when that range of CTP and HI values produced only two possible classifications. This allowed us to capture those cases when CTP and HI observations between the two platforms may have been nearly identical, but on opposite sides of a classification threshold. For example, if CTP observed by both platforms lies between 150 and 200 J kg^{-1} , but the observed HI for one platform is 9.5°C while the other is 10.2°C, then the former would be considered “wet advantage” while the latter would be considered “transition.” Thus, for the uncertainty analysis, if the AERI classification differed from that of the radiosonde initially, but the “correct” (radiosonde) classification was within the AERI's window of uncertainty, and that window of uncertainty only included two possible classifications, then that day would be counted as a “hit.” A summary of these methods can be found in Fig. 5.

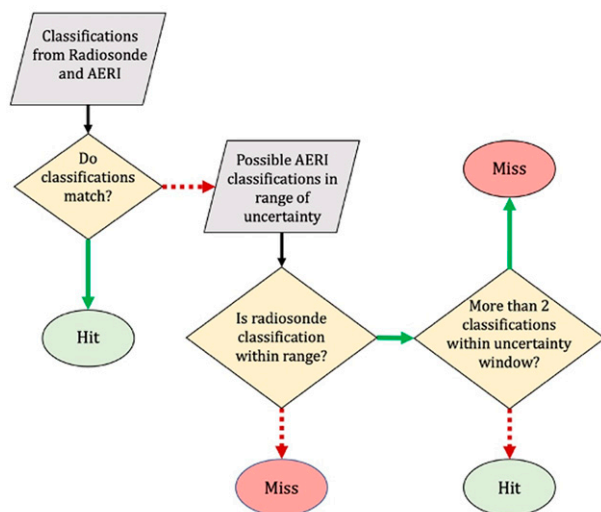


FIG. 5. Flowchart for computing contingency matrix with uncertainty. Green arrows represent “yes,” and red dashed arrows represent “no.”

AERI and radiosonde observations produced the same classification of atmospheric preconditioning approximately 71% of the time with an HSS of 0.62 (Fig. 4a). The majority of days were atmospherically controlled. For wet advantage and dry advantage days, the two platforms agreed just over half of the time, while transition days displayed more off-diagonal counts than counts along the diagonal. When we introduced a limited range of uncertainty (Fig. 4b), this resulted in agreement on 81% of days, while agreement on both wet and dry advantage days improved from just over half of days to over 75% of days. Transition days also displayed a tremendous improvement in agreement when considering uncertainty, increasing from 29% to 57% of days, and the HSS improved from 0.62 to 0.75. The movement of off-diagonal elements to the diagonal suggests that the reason for differences in the initial classification are likely driven by borderline CTP and HI values that were near the thresholds for a given pair of categories.

d. Temporal variability in CTP and HI

A second analysis examined the temporal variability in CTP and HI using only AERI observations. The motivation behind inspecting the temporal variability in these two quantities is driven by the potential differences across time zones in accumulated net radiation at upper-air stations during the morning upper-air observation. For example, during the summer, an upper-air station on the East Coast of the United States will have had two additional hours of downwelling shortwave radiation at 1200 UTC than an upper-air station at the same latitude within the mountain time zone. Therefore, it is important to ensure that the 1200 UTC radiosonde observation can still be employed in the computation of this coupling metric across time zones.

The high temporal resolution of the AERI enables this type of analysis. While the AERI is at a fixed location, evaluating

CTP and HI computed during time windows preceding and following the 1200 UTC radiosonde observation can be used to represent the accumulated net radiation in other time zones. We used the 1100 to 1200 UTC time window as “truth” because it corresponds to the 1200 UTC radiosonde observations. Hereinafter, this period is denoted as T12. Because the ARM central facility is located within the central time zone, accumulated net radiation in the mountain time zone at 1200 UTC would be 1 h behind the central time zone, or more similar to what is observed in the central time zone during the 1000–1100 UTC time window (hereinafter T11). Similarly, the eastern time zone would be 1 h ahead, or more similar to the accumulated net radiation at the central facility during the 1200–1300 UTC time window (T13).

Past applications of the framework (Ferguson and Wood 2011; Roundy et al. 2013; Roundy and Santanello 2017) have used vertical profiles obtained at times other than 1200 UTC such as those obtained from the Atmospheric Infrared Sounder (AIRS), which are acquired at approximately 0130 LT for a given location. As such, we also computed CTP and HI for the time window from 0700 to 0800 UTC (T08), which corresponds to the AIRS overpass time at 0130 CST (local time).

It is hypothesized that, in the absence of significant advective processes or the passage of synoptic-scale features, these two quantities should remain relatively constant in time. Further, even in those locations where the sun rises earlier, the PBL should not be fully developed to the levels where CTP and HI are measured.

The difference between CTP and HI at T12 (time window considered as truth) and the three other intervals were computed by subtracting the values at other times from the CTP and HI values at T12. All differences were statistically significant at $p < 0.05$ except for the CTP differences for T11–T12 and T11–T10. The difference distributions (Fig. 6) provide several key results:

- 1) HI at T11 and T13 displayed similar agreement with T12, while the HI values at T08 exhibited a much greater range of differences with T12 (Figs. 6a,c).
- 2) HI at T12 was slightly less than at T11 and slightly greater than at T13, and as such, the atmosphere slightly moistened over time (Figs. 6a,c). (Recall that higher values of HI correspond to greater dewpoint depressions).
- 3) Similarly, T08 displayed the greatest differences from T12 and a negative median difference indicates that HI at T08 was greater than at T12 (Fig. 6c). This remains consistent with T11 and T13 results that indicate that the atmosphere moistens with time.
- 4) HI at T11 and T13 had the lowest interquartile range (IQR) (Fig. 6c), with a majority of observations falling within 2°C of HI at T12, while the IQR for T08 was greater and a majority of T08 HI observations were within 6°C of those at T12.
- 5) CTP observations were relatively consistent for all three periods and displayed the same sign as biases to those observed in HI, with CTP observations at T13 being less than those at T12, while CTP observations at T11 and T08 were greater than those at T12 (Figs. 6b,d).

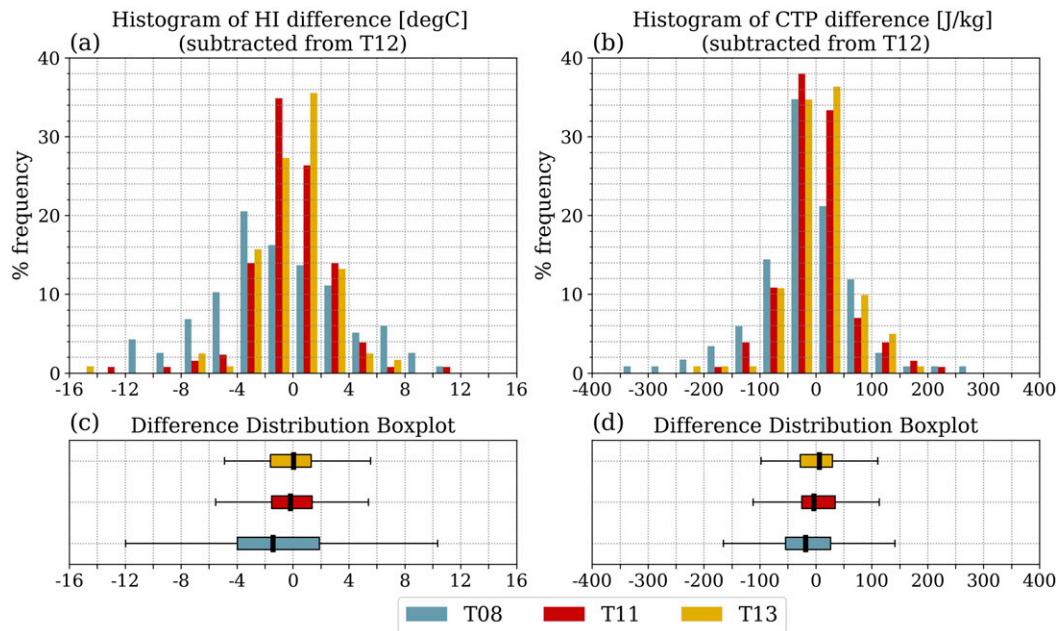


FIG. 6. Histogram of temporal differences between (a) HI and (b) CTP, and boxplots displaying median and interquartile range of temporal differences for (c) HI and (d) CTP computed for T12 – T08 (blue), T12 – T11 (red), and T12 – T13 (yellow).

- 6) The greatest differences in CTP were observed between T08 and T12 (Fig. 6d).
- 7) Most CTP observations at T08, T11, and T13 were within 100 J kg^{-1} of T12, with differences in T08 versus T12 having a greater IQR, or greater variability (Fig. 6d).

e. Composite vertical profiles

Composite mean profiles were computed to better understand where differences in CTP and HI were arising; CTP at each period of interest was subtracted from CTP at T12. From this difference distribution, composite mean temperature profiles on the three days with the greatest differences in CTP above the 95th percentile (Figs. 7a–c) and below the 5th percentile (Figs. 7d–f) were computed. Evaluating both tails of the distribution allowed us to evaluate whether there were truly large differences between conditions in which T12 was over- or underestimated or whether the differences were related to small changes in the vertical profile at certain levels, such as the height of an inversion rising or falling. When CTP at T12 is greater than CTP at other times, these differences are primarily associated with differences in lapse rates within the layer. Temperature profiles displayed similar temperatures at 100 hPa AGL, resulting in CTP parcel profiles being obtained for approximately the same moist adiabat. The profiles diverged above this level with steeper lapse rates observed for T12 contributing to more positive CTP than the comparison times. Conversely, when CTP at T12 was less than CTP at other times, steeper lapse rates were often observed for the comparison times.

Composite mean profiles were also computed for HI difference distributions (Fig. 8). The greatest differences in HI

were primarily driven by differences between dewpoint profiles while temperature profiles were markedly similar in time. An exception is those cases when HI at T12 was less than HI at T08 (Fig. 8d) where both temperature and dewpoint profiles differed among the two times. This confirms our hypothesis that the greater length of time between observations at T08 and T12 would allow for greater changes in temperature and moisture within the lower portions of the atmosphere. Even within the tails of the difference distributions, the differences in thermodynamic profiles are most pronounced at both levels in which HI is measured for T12–T08. The greatest contribution to differences in HI can be further narrowed down to differences in the dewpoint depression observations at 150 hPa AGL. Most profiles show relatively better agreement in dewpoint depression observations at 50 hPa AGL. The reasons for this are twofold. First, given the AERI's ability to represent CTP and HI well, it is likely that temperature and moisture profiles changed between the two times being compared. Second, while the AERI provides a good representation of reality, all observations include some degree of uncertainty. In this case, vertical resolution decreases with height, and it is likely that coarser vertical resolution is playing a role in the greater differences in dewpoint depression observed at 150 hPa AGL.

f. Temporal variability in preconditioning classifications

Even if median temporal differences in HI are close to 2°C and CTP median differences are approximately 100 J kg^{-1} , they still may lead to the same category for classification of preconditioning based on the CTP–HI framework as long as these differences do not straddle categorical thresholds.

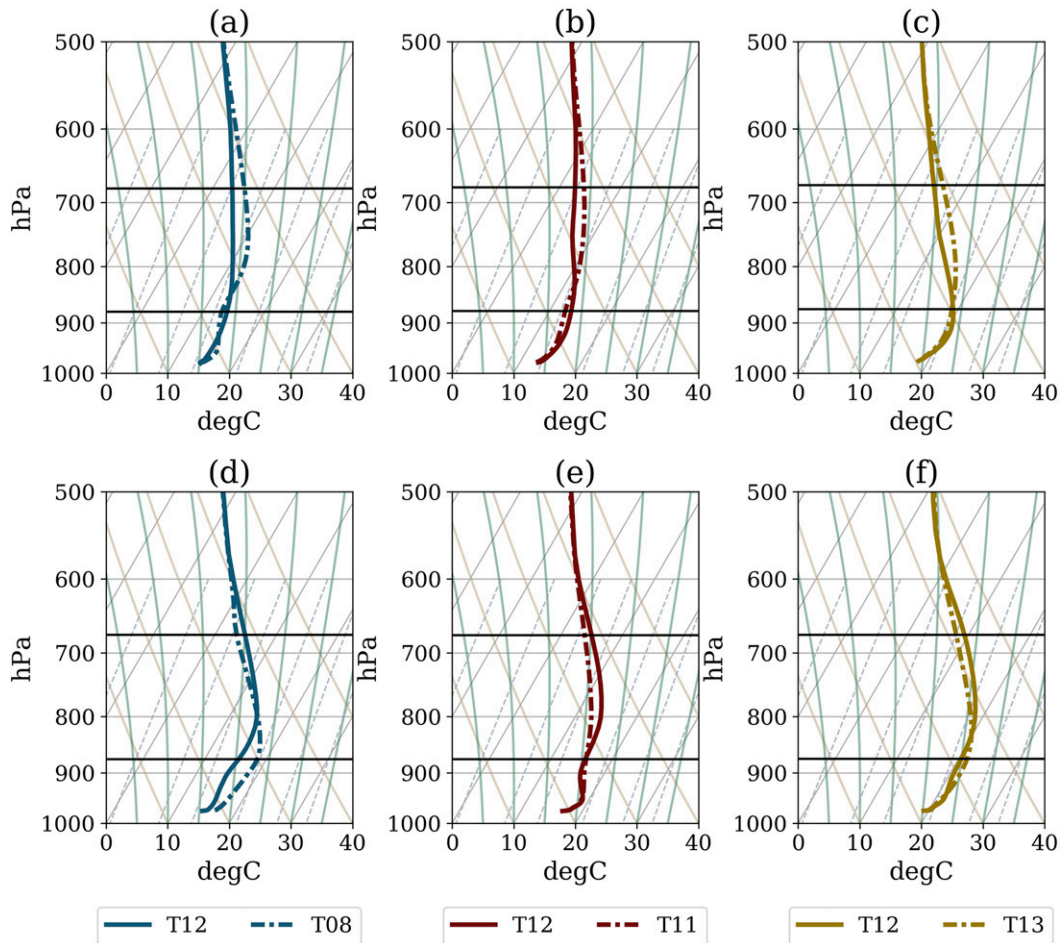


FIG. 7. Composite temperature profiles for days with the greatest temporal difference (CTP at T12 – CTP at T08, T11, and T13) in CTP for differences (a)–(c) above the 95th percentile and for differences (d)–(f) below the 5th percentile. Black horizontal lines represent the 100- and 300-hPa (AGL) levels.

Figure 9 shows contingency matrices of preconditioning classification categories at T12 versus T08 (Fig. 9a), T11 (Fig. 9b), and T13 (Fig. 9c), respectively, along with HSS. As in Fig. 4, the categories shown are a slight extension of the original framework as the atmospherically controlled category was broken into subcategories to discern whether atmospherically controlled scenarios were a result of enhanced stability (ACst), lack of moisture (ACd), or excess of moisture (ACw). Atmospherically controlled was the most common classification for all times, with the ACd subcategory occurring most frequently.

We looked for the greatest concentration of frequencies on the diagonal of each confusion matrix (Fig. 9), as that suggests both times agree on classification even when exact values of CTP and HI differ. Because T11 and T13 CTP and HI differed the least from T12, it is not surprising that these two times also displayed the greatest agreement in classifications with little difference in HSS and both agreeing with T12 during approximately 78% of days. Where CTP and HI differed most for the T08 case, the greatest frequency of

off-diagonal observations also occurred in the classification matrix (Fig. 9a). When T12 was classified as WA, T08 could be classified as any of the three nonatmospherically controlled classifications, though WA was still the most frequent classification. Overall, the same classification as T12 was produced by T08, T11, and T13 for 64%, 78%, and 79% of cases, respectively.

When classification differences occurred, these were often for adjacent categories with a clustering of off diagonal counts immediately adjacent to those along the diagonal. To further explore this, we performed the same uncertainty analysis that was used to compare the radiosonde and AERI observations, except that T12 (AERI) observations were considered “absolute truth” for this uncertainty analysis. Uncertainties were then computed at T08, T11, and T13 individually using each time’s distribution of potential profiles and applying the same uncertainty thresholds used in the radiosonde-versus-AERI analysis. Addition of uncertainty improved the percentage of days with agreement in time for all three times considered and also improved HSS for all three times (Fig. 10). The decrease in

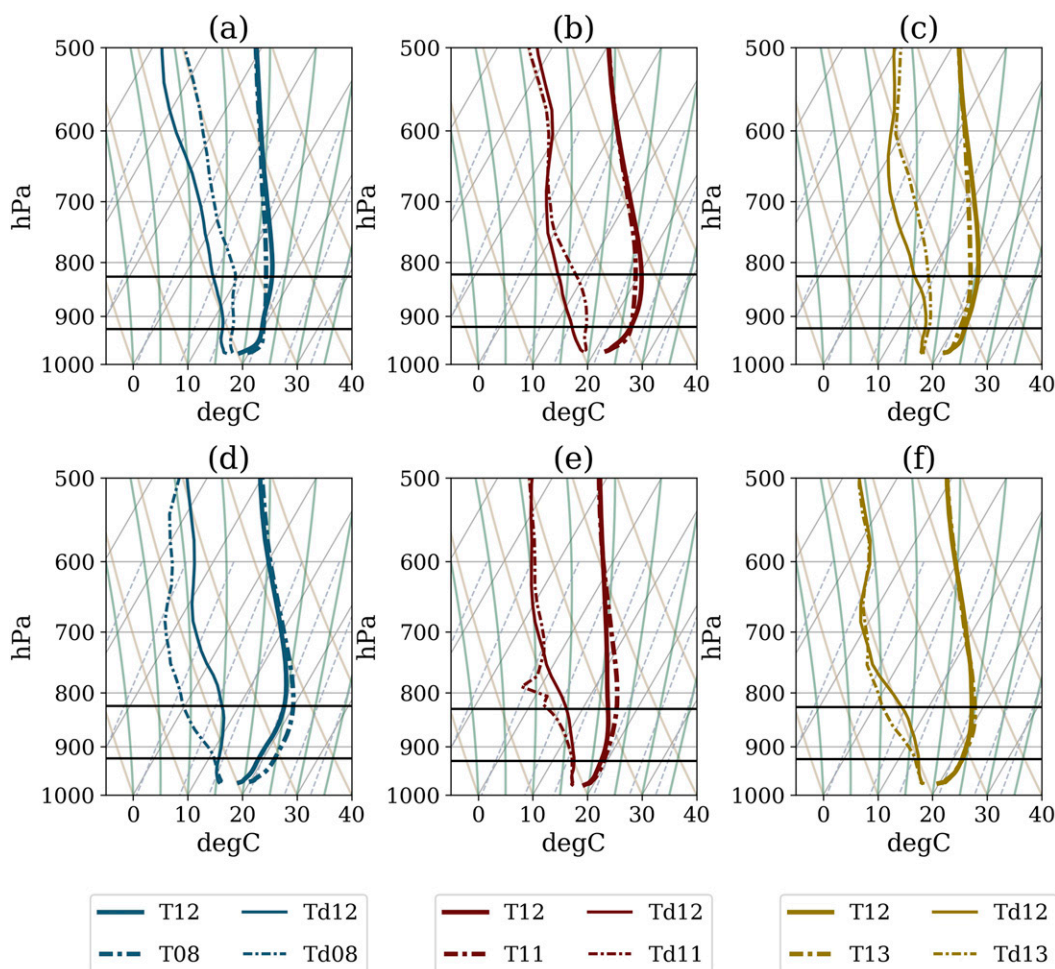


FIG. 8. As in Fig. 7, but for HI difference distributions and with the inclusion of dewpoint profiles. Horizontal black lines represent 50 and 150 hPa AGL, at which levels dewpoint depressions for HI computations are measured.

number of off-diagonal elements is especially apparent for T13 versus T12 (Fig. 10c).

When we looked instead at the frequency of each category by time, during the 2017 to 2019 period (Fig. 9d), and not at whether these were occurring on the same day, each time displayed similar frequencies per classification. ACd was observed less frequently at T13 than during the other periods, while ACw was observed most frequently for T13, further supporting the idea of atmospheric moistening with time. WA was the most common categorization for the nonatmospherically controlled days for all periods, while T and DA were similar in frequency for all time periods.

4. Discussion

In this study we demonstrated the utility of the AERI for observation-based land-atmosphere coupling analysis using the CTP-HI framework (Findell and Eltahir 2003a,b).

Our study was motivated by two primary questions:

- 1) What are the uncertainties associated with computing CTP and HI from radiosonde profiles versus from ground-based AERI-retrieved profiles?
- 2) Do CTP and HI exhibit substantial temporal variability overnight, or are these values consistent as long as they are obtained for a preconvective PBL?

We found that the AERI provides a realistic representation of CTP and HI and agreed well with radiosonde observations of the same metrics, even though small uncertainties were still present. These uncertainties were most apparent for the comparison of CTP values computed from radiosonde versus AERI thermodynamic profiles. These uncertainties are not surprising given CTP is a vertically integrated metric and it incorporates observations from higher levels in the atmosphere. Integrated metrics such as CTP or, in the case of Blumberg et al. (2017), CAPE have greater uncertainties than simpler metrics like HI. CTP measurements are also obtained at greater heights in the atmosphere (i.e., approximately 1–3 km) where vertical resolution of the AERI is reduced in

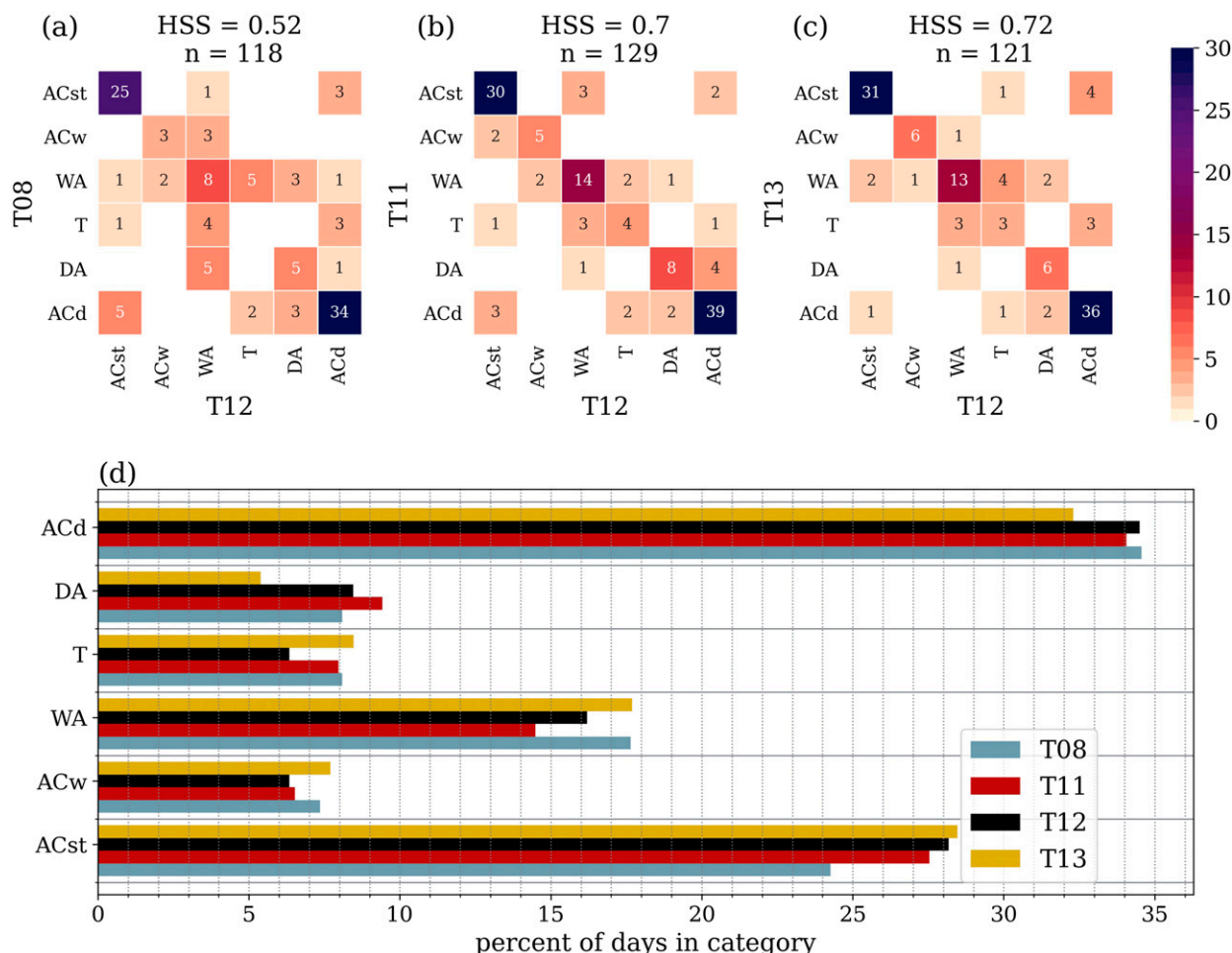


FIG. 9. Contingency matrix of classifications based on CTP and HI combinations for 1100–1200 UTC (+0 h) vs (a) 0600–0700 UTC (–5 h), (b) 1000–1100 UTC (–1 h), and (c) 1200–1300 UTC (+1 h). Abbreviations for each classification are provided in section 3a. (d) Percentage of days in each category for each time window.

comparison with HI measurements that are made lower in the atmosphere (i.e., approximately 0.5 and 1.5 km) where vertical resolution is greater.

The impact of vertical resolution on these uncertainties was further realized when radiosonde profiles were smoothed to the same resolution as AERI profiles. Comparison of profiles with the same vertical resolution produced greater agreement in observations of CTP and HI between the two observational platforms. This further suggests that vertical resolution is a significant driver of the difference between radiosonde- and AERI-derived CTP and HI. Although uncertainties exist, they do not hinder the AERI's ability to provide a realistic estimation of CTP and HI.

AERI and unsmoothed radiosonde diagnoses of atmospheric preconditioning based on the CTP–HI framework were identical for a majority of days, even if exact values of CTP and HI did not match. Incorporating uncertainty estimates further demonstrated the AERI's utility in applying the CTP and HI framework, producing a greater number of days in which both AERI and radiosonde profiles diagnosed the

same atmospheric preconditioning. Such analyses further confirm the hypothesis that a majority of the initial differences in preconditioning classification were driven by instances when radiosonde CTP and HI values were at the boundaries of a given category's threshold. This was made apparent by the increase in along diagonal elements within the uncertainty contingency matrix (Fig. 5), and a corresponding decrease in off-diagonal elements, especially within adjacent categories.

The agreement between AERI and radiosonde observations of CTP and HI demonstrated that the AERI can be useful for obtaining vertical profiles in time and space where radiosonde observations are lacking. The temporal frequency of AERI observations also provides a unique opportunity to explore the variability of this metric in time. Accumulated net radiation varies in space such that soundings released at the same UTC time do not coincide with the exact same PBL conditions around the world. We explored variability surrounding the 1200 UTC observation as this corresponds to the morning observation in much of the Western Hemisphere. It is

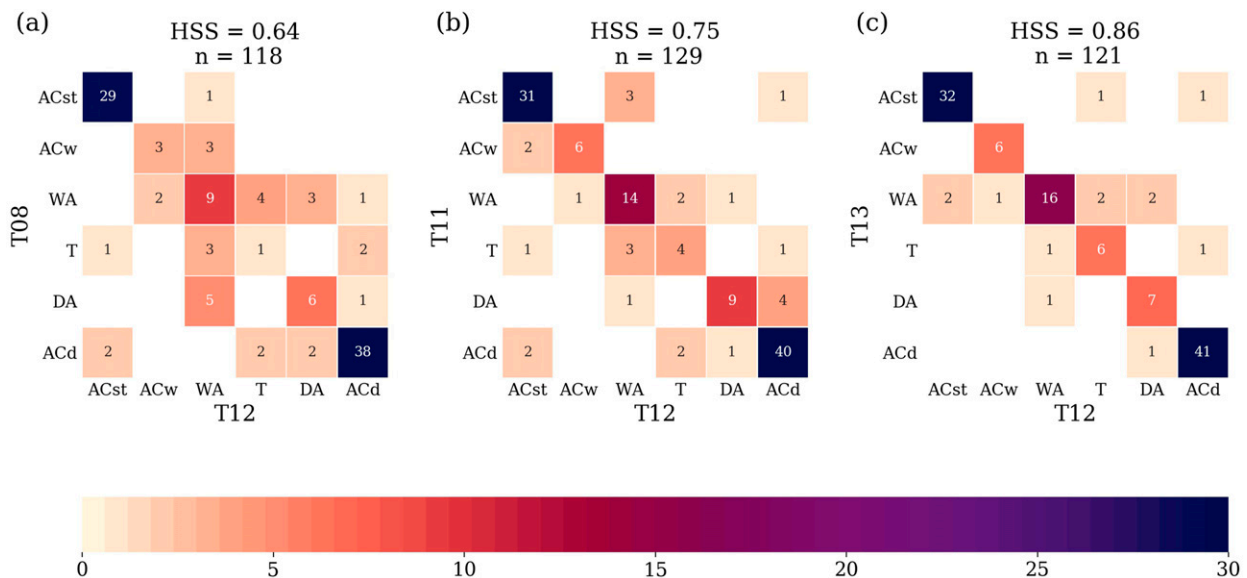


FIG. 10. As in Figs. 9a–c, but comparing classifications at T12 with those within windows of uncertainty for (a) T08, (b) T11, and (c) T13.

important to note that the implications of our results may be interpreted for locations in a different hemisphere, where the morning sounding may coincide with 0000 UTC. We are primarily concerned with variability in CTP and HI in the hours immediately preceding and following the hour of the morning sounding but we included an additional time period (0700–0800 UTC) in the analysis for comparison with past studies using the CTP–HI framework.

Our results suggest that variability in CTP and HI in the hours immediately surrounding the morning sounding is minimal. Composite mean profiles for the cases with the greatest temporal difference in CTP or HI indicate a greater variation in moisture profiles than temperature profiles with time at the levels in which CTP and HI are measured. This is important because it suggests that while CTP and HI are measured in portions of the atmosphere decoupled from the surface, the atmosphere continues to evolve. However, we recognize that the variation in moisture may also be unique to the Southern Great Plains location and future work could address this by performing similar studies using AERI observations outside of this region.

In general, as the difference in time from T12 increases, so do the differences in CTP and HI, and this is particularly true for T08 versus T12 observations. Even the most extreme differences, in the tails of the difference distributions, were more pronounced for T08. The composite profiles were obtained for extreme values in the difference distributions and these extreme cases were often associated with frontal passages, low-level jets, and other large-scale phenomena (not shown). The large differences that arose over time as a result of these meteorological influences suggest that computations of CTP and HI obtained from satellite remote sensing platforms near T08 may not always be a good approximation for atmospheric preconditioning. While median temporal differences in CTP and HI were often small, even small differences in values can

produce different classifications based on the original framework. Where T08 may diagnose the atmospheric preconditioning to be most favorable for convection over dry soils, T12 on the same day might diagnose the atmosphere as more favorable for convection over wet soils. Therefore, on a specific day, greater uncertainty in the diagnosis of atmospheric preconditioning may exist with vertical profiles obtained farther in time from the 1200 UTC observation window. T11 and T13 showed greater skill at producing the same preconditioning classification as T12, while T08 performed noticeably worse. Uncertainty estimates enhanced skill for all three times considered, suggesting that a reasonable estimate of atmospheric preconditioning can be obtained at times other than T12. Even so, when considering the categories that correspond to nonatmospherically controlled days, T08 displayed more off-diagonal elements for WA and T days despite incorporating a window of uncertainty. This likely reflects an actual difference in the atmospheric preconditioning between the two times, especially when T11 and T13 correctly identified such days at least half of the time when uncertainty windows were considered.

Even if CTP and HI observations at T08, T11, T12, and T13 were consistent with one another, synoptic-scale processes could alter the environment at any time between the morning sounding and afternoon period for which the CTP–HI framework diagnoses convective preconditioning. For example, if wet soils were observed and application of the framework diagnosed the morning atmosphere as being preconditioned for convection over wet soils on a day with an afternoon frontal passage, it would be difficult to forecast the relative contribution of the land surface from the contribution of large-scale drivers toward triggering convective precipitation using this metric alone. Thus, a primary limitation of our analysis is that we did not filter our data for synoptically quiescent days only as this would have adversely impacted our sample size, but it is

expected that doing so would result in even greater temporal agreement in CTP and HI values and greater predictive utility from those values. The thresholds provided by Findell and Eltahir (2003a,b) are meant to serve as guidelines and may be flexible based upon regional climatology (Wakefield et al. 2019).

5. Conclusions

The implications of this CTP-HI analysis are twofold. First, by showing good agreement between radiosonde and AERI observations of CTP and HI, we were able to evaluate the temporal variability in this coupling metric with confidence that the AERI retrievals are representative of reality. Second, we demonstrated some temporal variability in this metric within a given day, and applications of the framework are best suited to locations where the morning sounding corresponds to a local time within 1–2 h of the morning sounding time in the central time zone.

Days in which HI and CTP differed greatly are not likely to be the most favorable days for land–atmosphere interactions studies as large-scale meteorological influences contributed to substantial temporal evolution in temperature and moisture profiles. As such, synoptic influences on moisture and temperature would likely overpower the influence of the land surface. However, it is possible that looking at the temporal evolution of CTP and HI over a location could provide a means of identifying days that are favorable for land–atmosphere coupling and those that are not. Days in which CTP and HI exceed a certain difference threshold over time would be considered unfavorable for land–atmosphere interaction studies. This could be automated for identification of such days within a large dataset. Such an approach is beyond the scope of the current study, but future work could evaluate whether there is a variability threshold for days that are considered to be optimal for land–atmosphere coupling study versus days that are not.

Vertical profiles of temperature and moisture are often incorporated into land–atmosphere coupling metrics, which can limit their applicability from an observational perspective as the temporal and spatial coverage of atmospheric profiles is sparse. The AERI can be used in such locations to better observe land–atmosphere coupling, and these observations may also be used to verify model representation of land–atmosphere coupling in locations where such comparisons were not previously possible.

Acknowledgments. This work was supported by the Future Investigators in NASA Earth Space Science and Technology (FINESST) Award 80NSSC19K1365. This work was partially supported by the U.S. Department of Energy's Atmospheric System Research (ASR) program (Grant 89243019SSC000034) and by NOAA's Atmospheric Science for Renewable Energy (ASRE) program and National Science Foundation Grants OIA-1920946 and OIA-1946093.

Data availability statement. Datasets are available upon request from the author.

REFERENCES

- Andersen, T. K., and J. M. Shepherd, 2013: A global spatiotemporal analysis of inland tropical cyclone maintenance or intensification. *Int. J. Climatol.*, **34**, 391–402, <https://doi.org/10.1002/joc.3693>.
- , D. E. Radcliffe, and J. M. Shepherd, 2013: Quantifying surface energy fluxes in the vicinity of inland-tracking tropical cyclones. *J. Meteor. Appl. Climatol.*, **52**, 2797–2808, <https://doi.org/10.1175/JAMC-D-13-035.1>.
- Arndt, D. S., J. B. Basara, R. A. McPherson, B. G. Illston, G. D. Mcmanus, and D. B. Demko, 2009: Observations of the overland reintensification of Tropical Storm Erin (2007). *Bull. Amer. Meteor. Soc.*, **90**, 1079–1094, <https://doi.org/10.1175/2009BAMS2644.1>.
- Bakhshaii, A., and R. Stull, 2013: Saturated pseudoadiabats—A noniterative approximation. *J. Meteor. Appl. Climatol.*, **52**, 5–15, <https://doi.org/10.1175/JAMC-D-12-062.1>.
- Basara, J. B., and K. C. Crawford, 2002: Linear relationships between root-zone soil moisture and atmospheric processes in the planetary boundary layer. *J. Geophys. Res.*, **107**, 4274, <https://doi.org/10.1029/2001JD000633>.
- Blumberg, W. G., D. D. Turner, U. Löhnert, and S. Castleberry, 2015: Ground-based temperature and humidity profiling using spectral infrared and microwave observations. Part II: Actual retrieval performance in clear-sky and cloudy conditions. *J. Appl. Meteor. Climatol.*, **54**, 2305–2319, <https://doi.org/10.1175/JAMC-D-15-0005.1>.
- , T. J. Wagner, D. D. Turner, and J. Correia, 2017: Quantifying the accuracy and uncertainty of diurnal thermodynamic profiles and convection indices derived from the Atmospheric Emitted Radiance Interferometer. *J. Appl. Meteor. Climatol.*, **56**, 2747–2766, <https://doi.org/10.1175/JAMC-D-17-0036.1>.
- Dirmeyer, P. A., 2001: An evaluation of the strength of land–atmosphere coupling. *J. Hydrometeorol.*, **2**, 329–344, [https://doi.org/10.1175/1525-7541\(2001\)002<0329:AEOTSO>2.0.CO;2](https://doi.org/10.1175/1525-7541(2001)002<0329:AEOTSO>2.0.CO;2).
- , 2006: The hydrologic feedback pathway for land–climate coupling. *J. Hydrometeorol.*, **7**, 857–867, <https://doi.org/10.1175/JHM526.1>.
- , and S. Halder, 2016: Sensitivity of numerical weather forecasts to initial soil moisture variations in CFSv2. *Wea. Forecasting*, **31**, 1973–1983, <https://doi.org/10.1175/WAF-D-16-0049.1>.
- Ek, M. B., and L. Mahrt, 1994: Daytime evolution of relative humidity at the boundary layer top. *Mon. Wea. Rev.*, **122**, 2709–2721, [https://doi.org/10.1175/1520-0493\(1994\)122<2709:DEORHA>2.0.CO;2](https://doi.org/10.1175/1520-0493(1994)122<2709:DEORHA>2.0.CO;2).
- , and A. A. M. Holtslag, 2004: Influence of soil moisture on boundary layer cloud development. *J. Hydrometeorol.*, **5**, 86–99, [https://doi.org/10.1175/1525-7541\(2004\)005<0086:IOSMOB>2.0.CO;2](https://doi.org/10.1175/1525-7541(2004)005<0086:IOSMOB>2.0.CO;2).
- Emanuel, K., J. Callaghan, and P. Otto, 2008: A hypothesis for the redevelopment of warm-core cyclones over Northern Australia. *Mon. Wea. Rev.*, **136**, 3863–3872, <https://doi.org/10.1175/2008MWR2409.1>.
- Feltz, W. F., W. L. Smith, R. O. Knuteson, H. E. Revercomb, H. M. Woolf, and H. B. Howell, 1998: Meteorological applications of temperature and water vapor retrievals from the ground-based Atmospheric Emitted Radiance Interferometer (AERI). *J. Appl. Meteor.*, **37**, 857–875, [https://doi.org/10.1175/1520-0450\(1998\)037<0857:MAOTAW>2.0.CO;2](https://doi.org/10.1175/1520-0450(1998)037<0857:MAOTAW>2.0.CO;2).

- , —, H. B. Howell, R. O. Knuteson, H. Woolf, and H. E. Revercomb, 2003: Near-continuous profiling of temperature, moisture, and atmospheric stability using the Atmospheric Emitted Radiance Interferometer (AERI). *J. Appl. Meteor.*, **42**, 584–597, [https://doi.org/10.1175/1520-0450\(2003\)042<0584:NPOTMA>2.0.CO;2](https://doi.org/10.1175/1520-0450(2003)042<0584:NPOTMA>2.0.CO;2).
- Ferguson, C. R., and E. F. Wood, 2011: Observed land–atmosphere coupling from satellite remote sensing and reanalysis. *J. Hydrometeorol.*, **12**, 1221–1254, <https://doi.org/10.1175/2011JHM1380.1>.
- Findell, K. L., and E. A. B. Eltahir, 2003a: Atmospheric controls on soil moisture–boundary layer interactions. Part I: Framework development. *J. Hydrometeorol.*, **4**, 552–569, [https://doi.org/10.1175/1525-7541\(2003\)004<0552:ACOSML>2.0.CO;2](https://doi.org/10.1175/1525-7541(2003)004<0552:ACOSML>2.0.CO;2).
- , and —, 2003b: Atmospheric controls on soil moisture–boundary layer interactions. Part II: Feedbacks within the continental United States. *J. Hydrometeorol.*, **4**, 570–583, [https://doi.org/10.1175/1525-7541\(2003\)004<0570:ACOSML>2.0.CO;2](https://doi.org/10.1175/1525-7541(2003)004<0570:ACOSML>2.0.CO;2).
- Guo, Z., and Coauthors, 2006: GLACE: The Global Land–Atmosphere Coupling Experiment. Part II: Analysis. *J. Hydrometeorol.*, **7**, 611–625, <https://doi.org/10.1175/JHM511.1>.
- Irion, F. W., and Coauthors, 2018: Single-footprint retrievals of temperature, water vapor, and cloud properties from AIRS. *Atmos. Meas. Tech.*, **11**, 971–995, <https://doi.org/10.5194/amt-11-971-2018>.
- Jach, L., K. Warrach-Sagi, J. Ingwersen, E. Kaas, and V. Wulfmeyer, 2020: Land cover impacts on land-atmosphere coupling strength in climate simulations with WRF over Europe. *J. Geophys. Res. Atmos.*, **125**, e2019JD031989, <https://doi.org/10.1029/2019JD031989>.
- Knuteson, R. O., and Coauthors, 2004a: Atmospheric Emitted Radiance Interferometer. Part I: Instrument design. *J. Atmos. Oceanic Technol.*, **21**, 1763–1776, <https://doi.org/10.1175/JTECH-1662.1>.
- , and Coauthors, 2004b: Atmospheric Emitted Radiance Interferometer. Part II: Instrument performance. *J. Atmos. Oceanic Technol.*, **21**, 1777–1789, <https://doi.org/10.1175/JTECH-1663.1>.
- Koster, R. D., and Coauthors, 2004: Regions of strong coupling between soil moisture and precipitation. *Science*, **305**, 1138–1140, <https://doi.org/10.1126/science.1100217>.
- , and Coauthors, 2006: GLACE: The global land–atmosphere coupling experiment. Part I: Overview. *J. Hydrometeorol.*, **7**, 590–610, <https://doi.org/10.1175/JHM510.1>.
- , and Coauthors, 2011: The second phase of the Global Land–Atmosphere Coupling Experiment: Soil moisture contributions to subseasonal forecast skill. *J. Hydrometeorol.*, **12**, 805–822, <https://doi.org/10.1175/2011JHM1365.1>.
- , Y. Chang, and S. D. Schubert, 2014: A mechanism for land–atmosphere feedback involving planetary wave structures. *J. Climate*, **27**, 9290–9301, <https://doi.org/10.1175/JCLI-D-14-00315.1>.
- , —, H. Wang, and S. D. Schubert, 2016: Impacts of local soil moisture anomalies on the atmospheric circulation and on remote surface meteorological fields during boreal summer: A comprehensive analysis over North America. *J. Climate*, **29**, 7345–7364, <https://doi.org/10.1175/JCLI-D-16-0192.1>.
- May, R. M., S. C. Arms, P. Marsh, E. Bruning, J. R. Leeman, K. Goebbert, J. E. Thielen, and Z. Bruick, 2020: MetPy: A Python package for meteorological data. Unidata, <https://github.com/Unidata/MetPy>.
- McPherson, R. A., D. J. Stensrud, and K. C. Crawford, 2004: The impact of Oklahoma's winter wheat belt on the mesoscale environment. *Mon. Wea. Rev.*, **132**, 405–421, [https://doi.org/10.1175/1520-0493\(2004\)132<0405:TIOOWW>2.0.CO;2](https://doi.org/10.1175/1520-0493(2004)132<0405:TIOOWW>2.0.CO;2).
- Miralles, D. G., A. J. Teuling, C. C. V. Heerwaarden, and J. V.-G. D. Arellano, 2014: Mega-heatwave temperatures due to combined soil desiccation and atmospheric heat accumulation. *Nat. Geosci.*, **7**, 345–349, <https://doi.org/10.1038/ngeo2141>.
- Newsom, R. K., D. D. Turner, R. Lehtinen, C. Munkel, J. Kallio, and R. Roininen, 2020: Evaluation of a compact broadband differential absorption lidar for routine water vapor profiling in the atmospheric boundary layer. *J. Atmos. Oceanic Technol.*, **37**, 47–65, <https://doi.org/10.1175/JTECH-D-18-0102.1>.
- Phillips, T. J., and S. A. Klein, 2014: Land–atmosphere coupling manifested in warm-season observations on the U.S. Southern Great Plains. *J. Geophys. Res.*, **119**, 509–528, <https://doi.org/10.1002/2013JD020492>.
- Rodgers, C. D., 2000: *Inverse Methods for Atmospheric Sounding: Theory and Practice*. Series on Atmospheric, Oceanic and Planetary Physics, Vol. 2, World Scientific, 238 pp.
- Roundy, J. K., and J. A. Santanello, 2017: Utility of satellite remote sensing for land–atmosphere coupling and drought metrics. *J. Hydrometeorol.*, **18**, 863–877, <https://doi.org/10.1175/JHM-D-16-0171.1>.
- , C. R. Ferguson, and E. F. Wood, 2013: Temporal variability of land–atmosphere coupling and its implications for drought over the Southeast United States. *J. Hydrometeorol.*, **14**, 622–635, <https://doi.org/10.1175/JHM-D-12-090.1>.
- Santanello, J. A., Jr., C. D. Peters-Lidard, and S. V. Kumar, 2011a: Diagnosing the sensitivity of local land–atmosphere coupling via the soil moisture–boundary layer interaction. *J. Hydrometeorol.*, **12**, 766–786, <https://doi.org/10.1175/JHM-D-10-05014.1>.
- , and Coauthors, 2011b: Results from local land-atmosphere coupling (LoCo) project. *GEWEX News*, Vol. 21, No. 4, International GEWEX Project Office, Silver Spring, MD, 7–9, www.gewex.org/gewex-content/files_mf/1432209597Nov2011.pdf.
- , and Coauthors, 2018: Land–atmosphere interactions: The LoCo perspective. *Bull. Amer. Meteor. Soc.*, **99**, 1253–1272, <https://doi.org/10.1175/BAMS-D-17-0001.1>.
- Schumacher, D. L., J. Keune, C. C. V. Heerwaarden, J. V.-G. D. Arellano, A. J. Teuling, and D. G. Miralles, 2019: Amplification of mega-heatwaves through heat torrents fuelled by upwind drought. *Nat. Geosci.*, **12**, 712–717, <https://doi.org/10.1038/s41561-019-0431-6>.
- Seneviratne, S. I., D. Lüthi, M. Litschi, and C. Schär, 2006: Land–atmosphere coupling and climate change in Europe. *Nature*, **443**, 205–209, <https://doi.org/10.1038/nature05095>.
- Sisterson, D. L., R. A. Peppler, T. S. Cress, P. J. Lamb, and D. D. Turner, 2016: The ARM Southern Great Plains (SGP) site. *The Atmospheric Radiation Measurement Program: The First 20 Years*, Meteor. Monogr., No. 57, Amer. Meteor. Soc., <https://doi.org/10.1175/AMSMONOGRAPHS-D-16-0004.1>.
- Smith, W. L., W. F. Feltz, R. O. Knuteson, H. E. Revercomb, H. M. Woolf, and H. B. Howell, 1999: The retrieval of planetary boundary layer structure using ground-based infrared spectral radiance measurements. *J. Atmos. Oceanic Technol.*, **16**, 323–333, [https://doi.org/10.1175/1520-0426\(1999\)016<0323:TROPBL>2.0.CO;2](https://doi.org/10.1175/1520-0426(1999)016<0323:TROPBL>2.0.CO;2).
- Song, H.-J., C. R. Ferguson, and J. K. Roundy, 2016: Land–atmosphere coupling at the Southern Great Plains Atmospheric

- Radiation Measurement (ARM) field site and its role in anomalous afternoon peak precipitation. *J. Hydrometeor.*, **17**, 541–556, <https://doi.org/10.1175/JHM-D-15-0045.1>.
- Tang, Q., S. Xie, Y. Zhang, T. J. Phillips, J. A. Santanello, D. R. Cook, L. D. Riihimäki, and K. L. Gaustad, 2018: Heterogeneity in warm-season land-atmosphere coupling over the U.S. Southern Great Plains. *J. Geophys. Res. Atmos.*, **123**, 7867–7882, <https://doi.org/10.1029/2018JD028463>.
- Turner, D. D., and U. Löhnert, 2014: Information content and uncertainties in thermodynamic profiles and liquid cloud properties retrieved from the ground-based Atmospheric Emitted Radiance Interferometer (AERI). *J. Appl. Meteor. Climatol.*, **53**, 752–771, <https://doi.org/10.1175/JAMC-D-13-0126.1>.
- , and W. G. Blumberg, 2019: Improvements to the AERIoe thermodynamic profile retrieval algorithm. *IEEE Sel. Top. Appl. Earth Obs. Remote Sens.*, **12**, 1339–1354, <https://doi.org/10.1109/JSTARS.2018.2874968>.
- Wagner, T. J., W. F. Feltz, and S. A. Ackerman, 2008: The temporal evolution of convective indices in storm-producing environments. *Wea. Forecasting*, **23**, 786–794, <https://doi.org/10.1175/2008WAF2007046.1>.
- Wakefield, R. A., J. B. Basara, J. C. Furtado, B. G. Illston, C. R. Ferguson, and P. Klein, 2019: A modified framework for quantifying land–atmosphere covariability during hydrometeorological and soil wetness extremes in Oklahoma. *J. Meteor. Appl. Climatol.*, **58**, 1465–1483, <https://doi.org/10.1175/JAMC-D-18-0230.1>.
- , —, J. M. Shepherd, N. Brauer, J. C. Furtado, J. A. Santanello, and R. Edwards, 2021: The inland maintenance and re-intensification of Tropical Storm Bill (2015). Part I: Contributions of the brown ocean effect. *J. Hydrometeor.*, <https://doi.org/10.1175/JHM-D-20-0150.1>, in press.
- Wei, J., H. Su, and Z.-L. Yang, 2015: Impact of moisture flux convergence and soil moisture on precipitation: A case study for the southern United States with implications for the globe. *Climate Dyn.*, **46**, 467–481, <https://doi.org/10.1007/s00382-015-2593-2>.
- Wilks, D. S., 2011: *Statistical Methods in the Atmospheric Sciences*. 3rd ed. Elsevier, 676 pp.
- Wulfmeyer, V., and Coauthors, 2018: A new research approach for observing and characterizing land–atmosphere feedback. *Bull. Amer. Meteor. Soc.*, **99**, 1639–1667, <https://doi.org/10.1175/BAMS-D-17-0009.1>.